Mon. Not. R. Astron. Soc. **000**, 1–12 (2005) Printed 5 February 2008 (MN LaTeX style file v2.2)

arXiv:astro-ph/0605704v1 29 May 2006

On the Rees-Sciama effect: maps and statistics

N. Puchades[1] M.J. Fullana[2] J.V. Arnau[3] and D. Sáez[1]⋆
[1] *Departamento de Astronomía y Astrofísica, Universidad de Valencia. 46100 Burjassot, Valencia, Spain*
[2] *Institut de Matemàtica Multidisciplinar, Universitat Politècnica de València. 46022 València, Spain*
[3] *Departamento de Matemática Aplicada, Universidad de Valencia. 46100 Burjassot, Valencia, Spain*

5 February 2008

ABSTRACT

Small maps of the Rees-Sciama (RS) effect are simulated by using an appropriate N-body code and a certain ray-tracing procedure. A method designed for the statistical analysis of cosmic microwave background (CMB) maps is applied to study the resulting simulations. These techniques, recently proposed –by our team– to consider lens deformations of the CMB, are adapted to deal with the RS effect. This effect and the deviations from Gaussianity associated to it seem to be too small to be detected in the near future. This conclusion follows from our estimation of both the RS angular power spectrum and the RS reduced n-direction correlation functions for $n \leqslant 6$.

Key words: cosmic microwave background—cosmology:theory— large-scale structure of the universe—methods:numerical— methods:N-body simulations.

1 INTRODUCTION

From decoupling to present time, Cosmic Microwave Background (CMB) photons have been traveling –almost freely– through a homogeneous and isotropic background universe with small perturbations. Taking into account the main results from the analysis of the first year WMAP (Wilkinson Microwave Anisotropy Probe) data, which were presented in Bennet et al. (2003), it is assumed: (i) a Gaussian distribution of adiabatic energy density fluctuations with Zel'dovich spectrum, (ii) a currently accelerated expansion with reduced Hubble constant $h = 10^{-2} H_0 = 0.71$ (H_0 being the Hubble constant in units of $Km\ s^{-1} Mpc^{-1}$), (iii) a cosmological constant with density parameter $\Omega_\Lambda = 0.73$ producing the current acceleration, and (iv) cold dark matter (baryonic matter) with density parameter $\Omega_d = 0.23$ ($\Omega_b = 0.04$); hence, the total matter density parameter is $\Omega_m = \Omega_b + \Omega_d = 0.27$. In other words, a realization of the so-called concordance model is assumed and, then, the CMBFAST code (Seljak & Zaldarriaga 1996) is used to get the linearly evolved power spectrum, $P(k)$, of the scalar energy density fluctuations, which is defined by the relation $\langle \delta(\vec{k})\ \delta^*(\vec{k}') \rangle = (2\pi)^3 P(k) \delta(\vec{k} - \vec{k}')$. This spectrum is normalized with the condition $\sigma_8 = 0.93$ to have the required density of galaxy clusters (Eke, Cole & Frenk 1996).

Along this paper, units are chosen in such a way that the speed of light is $c = 1$ and the gravitation constant is $G = 1/8\pi$. Whatever quantity "A" may be, $A_{_L}$, A_0, and $A_{_B}$ stand for the A values on the last scattering surface, at present time, and in the background, respectively. Symbols $\vec{x}$, a, z, and η, stand for the comoving position vector, the scale factor, the redshift, and the conformal time, respectively. Condition $a_0 = 1\ Mpc$ is assumed.

Cosmological structures (scalar modes) produce a peculiar gravitational potential $\phi(\vec{x}, \eta)$ which interacts with the CMB. The partial time derivative of $\phi(\vec{x}, \eta)$ produces temperature fluctuations. Quantity $\Delta T/T_{_B} = (T - T_{_B})/T_{_B}$ measures fluctuations with respect to the CMB averaged temperature $T_{_B}$. This quantity is given by the formula:

$$\frac{\Delta T}{T_{_B}}(\vec{n}) = 2 \int_{\eta_{_L}}^{\eta_0} \frac{\partial \phi(\vec{x}, \eta)}{\partial \eta} d\eta \ , \tag{1}$$

where the integral is to be performed along the null geodesic of the perturbed universe associated to the observation direction $\vec{n}$. As it is well known, a good approximation to $\Delta T/T_{_B}$ can be obtained by calculating this integral along the background null geodesic corresponding to $\vec{n}$, which obeys the equation

$$x^i = \lambda(z) n^i \ , \tag{2}$$

where

$$\lambda(z) = H_0^{-1} \int_0^z \frac{db}{[\Omega_m (1+b)^3 + \Omega_\Lambda]^{1/2}} \ . \tag{3}$$

In the flat universe with cosmological constant we are considering, linear, mildly non-linear, and strongly non-linear structures contribute to the integral in Eq. (1). Indeed, this integral allows us to estimate the anisotropy produced by the total time varying peculiar gravitational potential of the universe. This anisotropy could be considered as an unique ef-

---

⋆ E-mail: diego.saez@uv.es (DS)

fect; nevertheless, the contributions –to the integral– due to linear and non-linear structure evolution are usually called the Integrated Sachs-Wolfe (ISW) and the Rees-Sciama (RS) effect, respectively. Some comments about this distinction seem to be worthwhile. During linear evolution, the peculiar potential can be written in the form $\phi_L D_1(a)/a$, where ϕ_L is the initial potential (taken at decoupling time) and $D_1(a)$ is the linear growth function for the density contrast. At any time, the total peculiar potential, ϕ, can be splitted as follows:

$$\phi = \phi_L \frac{D_1(a)}{a} + \phi_{NL} \ , \tag{4}$$

where ϕ_{NL} is the part of the potential properly due to nonlinear evolution. After substitution in Eq. (1) and integration until present time, the first term of the r.h.s. of this equation gives the ISW effect, whereas the second one is the source of the RS effect. Equation (4) leads to a consistent definition of both effects (the addition is the total integrated gravitational effect). Before the beginning of the nonlinear regime, function ϕ_{NL} takes on negligible second order values and only the ISW anisotropy can be significant. During the nonlinear regime, the first term continues contributing to the ISW effect and the second term produces the RS anisotropy. Let us now study the ratio $D_1(a)/a$ to discuss in more detail ISW anisotropy production in the concordance model, in which, function D_1 can be written as follows (in terms of z):

$$D_1(z) \propto \frac{1}{x}\left[\frac{2}{x}+x^2\right]^{1/2}\int_0^x \left[\frac{2}{y}+y^2\right]^{-3/2} dy \ , \tag{5}$$

where

$$x = \left[\frac{2\Omega_\lambda}{\Omega_m}\right]^{1/3}(1+z)^{-1} \ . \tag{6}$$

With the appropriate normalization factor, function D_1 is almost identical to the scale factor a for $z > 3$, whereas it is greater than this factor for $z < 3$. This behaviour is shown in Fig. (1), where we see that function D_1/a is very close to (greater than) unity for $z > 3$ ($z < 3$). Two periods can be then distinguished: in the first one ($z > 3$), the term $\phi_L D_1(a)/a$ is almost constant and no significant ISW anisotropy is generated. In the second period ($z < 3$), the potential $\phi_L D_1(a)/a$ varies and the ISW effect is produced. These facts can be easily understood. For $z > 3$, vacuum energy is subdominant and the concordance model approximately evolves as a flat universe without cosmological constant; in which, it is well known that no ISW is generated because the relation $D_1(a) \simeq a$ is satisfied. All the ISW effect is produced when vacuum energy plays a significant role in the evolution of the universe; namely, for $z < 3$; therefore, in the concordance model, the ISW and the RS effects are both produced at low redshifts. Only a small contribution to the RS effect is produced at $z > 3$ as a result of the first stages of non-linear evolution. The main part of the RS effect and all the ISW anisotropy are simulataneously generated at redshifts $z < 3$. The ISW (RS) effect dominates for small (large) enough multipoles (see next sections).

Since the location of the first peak of the CMB angular power spectrum indicates that the background universe is almost flat and, in such a case, the ISW effect only appears in the presence of vacuum energy (cosmological constant), any detection of the ISW effect could be considered as an indirect detection of vacuum energy. Since the largest ISW multipoles correspond to small ℓ values with large cosmic variances, a direct detection based on the analysis of CMB maps becomes problematic Hu & Dodelson (2002); nevertheless, ten years ago, Crittenden & Turok (1996) proposed an indirect detection method which is based on the estimate of cross-correlations between the CMB maps and tracers of the matter density distribution at $z < 3$ (risponsable for the ISW anisotropy). Many papers have been devoted to try this indirect detection (Fosalba, Gaztañaga & Castander (2003); Fosalba & Gaztañaga (2004); Boughn & Crittenden (2004); Afshordi, Lho & Strauss (2004); Nolta et al. (2004); Vielva, Martínez-González & Tucci (2006)); nevertheless, in the present paper, the ISW effect is only considered with the essential aim of estimating its contribution to our maps of the integrated gravitational effect, which are obtained from Eq. (1) and appropriate numerical techniques (see below). Since the ISW contribution is proved to be small enough (see next sections), our maps can be considered as approximated simulations of the RS effect; by this reason, these maps are hereafter called RS maps and the spectra extracted from them are considered as an approximation to the RS spectrum.

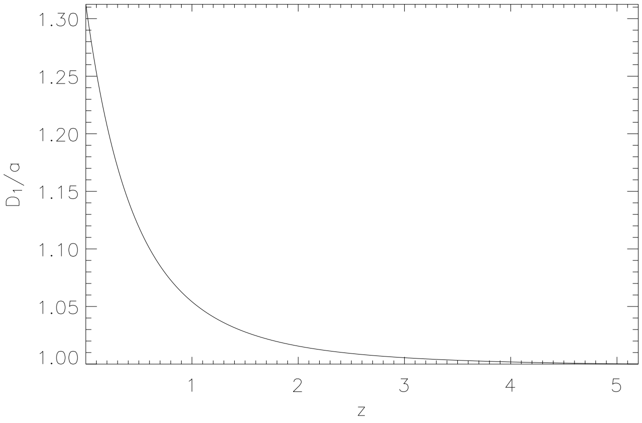

Figure 1. Ratio D_1/a as a function of z in the concordance model

This paper is organized as follows: Appropriate comments on the ISW effect are given in section 2. The numerical methods used to simulate maps of the RS effect are described in section 3. The RS angular power spectrum obtained from small maps is described in section 4, where the importance of the smallness of the maps (as a source of uncertainty) is discussed in detail. Next section deals with the estimation of both reduced m-correlations and deviations from Gaussianity and, finally, section 6 contains a summary of conclusions and a general discussion.

2 ON THE ANGULAR POWER SPECTRUM OF THE ISW EFFECT

In a flat background with cosmological constant, the angular power spectrum of the ISW effect depends on various parameters. The values of h, Ω_Λ, and σ_8 are particularly important. This spectrum has been previously calculated in various cases, see, e.g. Hu & Dodelson (2002); Cooray (2002).

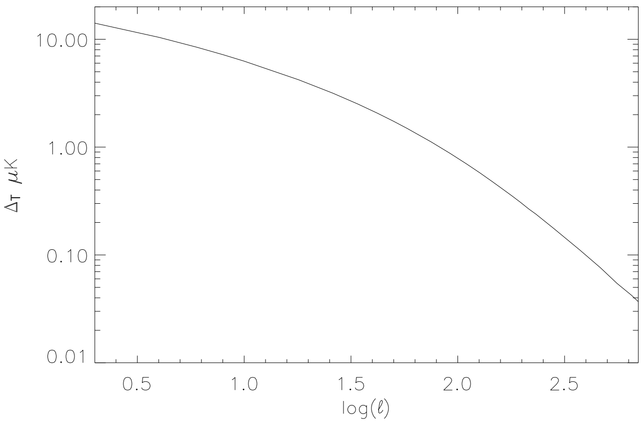

Figure 2. ISW power spectrum, Δ_T, in μK, as a function of $\log(\ell)$.

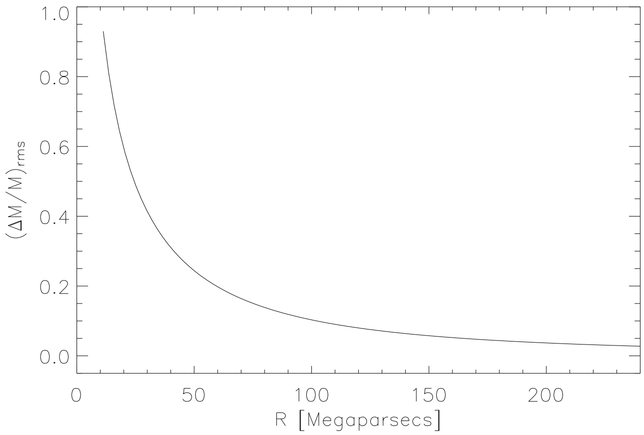

Figure 3. rms relative mass fluctuations inside a sphere whose present radius in Megaparsecs is R.

Here, it is calculated for the cosmological model and parameters fixed in the introduction. The C_ℓ quantities of the ISW effect can be written as follows (Fullana & Sáez 2000):

$$C_\ell = N \int_0^\infty \frac{P(k)}{k^2} \xi_\ell^2(k) dk \ , \tag{7}$$

where

$$\xi_\ell(k) = \int_{\lambda_0}^{\lambda_L} j_\ell[\lambda k] \frac{d}{d\lambda} \left[(1+z) D_1(z)\right] d\lambda \ , \tag{8}$$

j_ℓ being the spherical Bessel function of order ℓ, and

$$N = \frac{18 H_0^4}{\pi} \left[\frac{\Omega_m}{D_1(0)}\right]^2 \ , \tag{9}$$

where function $D_1(z)$ is given by Eqs. (5) and (6). The integrals in Eqs. (7) and (8) have been numerically calculated to get the required spectrum. Results are presented in Fig. (2), where quantity $\Delta_T = [\ell(\ell+1)C_\ell/2\pi]^{1/2}$ in μK (used along the paper to describe the angular power spectrum) is displayed in the ℓ interval [2,700].

Our estimation, as well as previous ones (see e.g. Hu & Dodelson (2002); Cooray (2002); Padmanabhan et al. (2005)), leads to two main conclusions: (1) the most important part of the ISW effect is produced by very large spatial scales (small k values) contributing to small multipoles, and (2) the contribution to this effect strongly decreases as the spatial scale does. For the parameters we have assumed, the Δ_T value corresponding to $\ell = 700$ is 0.037 μK and, moreover, quantity Δ_T rapidly decreases as ℓ increases reaching a value close to 0.0045 μK for $\ell \sim 2000$. These values are to be compared with those extracted from our numerically simulated maps. As a technical requirement associated to ray-tracing (see below), our maps are produced by the total time varying peculiar potential due to all the scales smaller than 60 Mpc, which are evolved by N-body simulations from redshift 5.2 to present time; hence, all the ISW effect produced (at $z < 3$, see Fig. (1)) by these scales is included in the resulting maps. The effect produced by scales greater than 60 Mpc must be independently calculated. Is it a pure ISW effect? A few considerations about linearity are useful to answer this question.

In order to discuss about linearity in detail, the root mean square (rms) of the relative mass fluctuations inside a sphere having a present radius of R Mpc (randomly placed in our flat universe) is estimated. Condition $a_0 = 1$ implies that number R is also the comoving radius of the sphere. This rms value is $\sigma(R) = (\Delta M/M)_{rms} = \langle(\delta M/M)^2\rangle^{1/2}$, with

$$\langle(\delta M/M)^2\rangle = \frac{1}{2\pi^2} \int_0^\infty k^2 P(k) W^2(kR) dk \ , \tag{10}$$

where $W(kR)$ is the window function of the R-sphere $[W(kR) = \frac{3}{y^3}(\sin y - y \cos y)$ with $y = kR$; see Peebles (1980)]. Numerical calculations based on these formulae lead to the $\sigma(R)$ values presented in Fig. 3. From this figure it follows that, for the chosen normalization of $P(k)$ and the comoving radius $R = 15$ Mpc, the σ_{15} value is close to 0.7; hence, it can be assumed (standard point of view) that regions having a comoving diameter greater than 30 Mpc can be treated as linearly evolving zones. The scale $\hat{L} = 60$ Mpc, used along this paper, evolves in the linear regime with $\sigma(30) \simeq 0.4$; hence, scales greater than 60 Mpc would produce a pure ISW effect to be separately estimated with appropriate linear techniques. The ISW effect produced by all the scales smaller than 60 Mpc is included in our maps and, obviously, it is smaller than the total ISW effect (see Fig. 2 and previous comments).

3 NUMERICAL METHODS

RS is a pure gravitational effect and, consequently, only the dominant dark matter component is considered, whereas the sub-dominant baryonic component is neglected. On account of these facts, the formation and evolution of non-linear cosmological structures can be described by using N-body simulations with appropriate boxes and resolutions. In the PM simulations we use here (Hockney & Eastwood 1988; Quilis, Ibáñez & Sáez 1998), the peculiar potential satisfies the equation (Martínez-González, Sanz & Silk 1990):

$$\Delta\phi = \frac{1}{2} a^2 (\rho_m - \rho_{mB}) \ . \tag{11}$$

The universe is assumed to be covered by simulation boxes and, consequently, it is periodic. As it was pointed out by Cerdá-Durán, Quilis & Sáez (2004) and Antón et al. (2005), periodicity effects magnify lens deformations and, in general, gravitational anisotropies as the RS effect. Various techniques (ray-tracing methods) have been used to avoid this magnification, for example, Tuluie, Laguna & Anninos (1996) averaged the temperature contrasts of many rays, but then, they found a map with too large pixels, from which, the multipoles corresponding to $\ell > 700$ could not be obtained. Another method based on multiple plane projections was proposed and applied to study week lensing by cosmological structures (see Jain, Seljak & White (2000) for a detailed description). Afterwards, White & Hu (2001) designed the "tiling" ray tracing procedure, in which, independent simulations with appropriate boxes and resolutions tile the photon trajectories. Finally, another method based on the existence of preferred directions and on the use of an appropriate cutoff was recently proposed and applied (Cerdá-Durán, Quilis & Sáez (2004); Antón et al. (2005)). In the required cutoff, the Fourier modes corresponding to spatial scales larger than a given one (L_{max}) are eliminated from the peculiar gravitational potential. The L_{max} value is chosen in such a way that: (a) the cutoff eliminates all the spatial scales which are too large to be well described in the simulation box, and (b) after the cutoff is performed, CMB photons cross neighbouring boxes through statistically independent regions. This cutoff is only performed in the output peculiar gravitational potential with the essential aim of calculating the integral in Eq. (1); however, all the spatial scales allowed by the box size are taken into account in the N-body simulation. Our ray-tracing method is a very good choice presenting some advantages with respect to other techniques (see Antón et al. (2005)), e.g., there are no discontinuities at the crossing points between successive boxes, the computational cost is moderated, and so on.

In order to study the RS effect, we develop the same type of N-body simulations which were used, in Antón et al. (2005), to deal with lensed maps of the CMB. In this way, various maps of the relative temperature variations due to the RS effect are created and analyzed, and the dependence of the results on various parameters involved in the simulations and also in their statistical analysis is then discussed. Most maps are regularly pixelised, but some maps based on HEALPIx (*Hierarchical Equal Area Isolatitude Pixelisation of the Sphere*, see Górski, Hivon & Wandelt (1999)) are also considered. Taking into account that the box size used in the mentioned N-body simulations (see Antón et al. (2005) for details) is $L = 256$ *Mpc*, and also that the main part of the RS effect is assumed to be produced at redshift $z < 5.2$ (see below), the size of the resulting RS maps appears to be close to 2°. Simulation boxes cover a periodic universe and, for the direction $\theta = 77.2^\circ$ and $\phi = 12.6^\circ$ (where θ and ϕ are spherical coordinates defined with respect to the box edges), the CMB photons cross around 30 boxes before passing through the region where they were initially located (in the first box). It can be verified that these boxes cover the trajectory of the CMB photons from the redshift $z_{in} \simeq 5.2$ to present time, and also that these photons cross successive boxes through independent regions separated by a distance close to 52 *Mpc*. The cutoff is performed at the scale $k_{min} = 2\pi/L_{max}$ with $L_{max} = 60$ *Mpc* (in agreement with previous comments about the scales involved in our simulations).

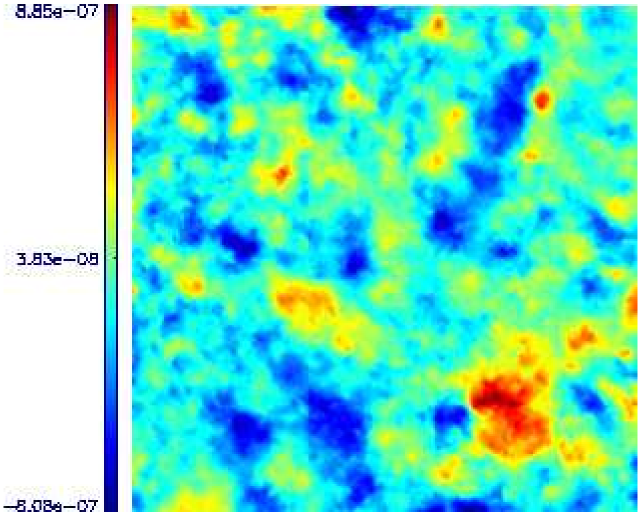

Figure 4. Simulated $1.83^\circ \times 1.83^\circ$ map of the RS effect obtained from a HR N-body simulation

Along the paper we develop three types of N-body simulations in boxes of L *Mpc* (integer and even L): Low Resolution (LR) simulations involving $L/2$ cells per edge and $(L/2)^3$ particles (2 *Mpc* cell size and $\sim$ 380 time steps), Intermediate Resolution (IR) simulations using L cells per edge and L^3 particles (1 *Mpc* cell size and $\sim$ 410 time steps), and High Resolution (HR) simulations with $2L$ cells per edge and $(2L)^3$ particles (0.5 *Mpc* cell size and $\sim$ 500 time steps). Figure (4) shows a RS map which has been obtained with our ray-tracing method and a HR simulation of structure. Its look is promising, but the correlations appearing in this type of maps must be estimated to get objective conclusions. It is done in next sections.

For any observation direction $\vec{n}$, function $\partial\phi/\partial\eta$ must be calculated in a set of points to estimate the integral in Eq. (1). We have chosen equidistant points (on the corresponding background geodesic) separated by a comoving distance equal to the cell size. Each of these points has a comoving position vector $\vec{x}_P$, and the photon passes by this position at time η_P. Point P is placed inside a certain P-cell of the computational grid and time η_P belongs to some interval $[\eta_i, \eta_{i+1}]$, where η_i and η_{i+1} are two successive times of the N-body simulation, at which, the peculiar potential ϕ is found at any grill node. The potential at point P is calculated at times η_{i-1}, η_i, η_{i+1}, and η_{i+2}. The calculation at any of these times is performed by means of a suitable 3D interpolation, which uses the potential in the vertices of the P-cell and in those of the neighbouring ones. From the resulting potential at the above four times, the partial derivative $\partial\phi/\partial\eta$ is finally calculated with an appropriated numerical method. For each type of N-body simulations (LR, IR or HR), various methods for spatial interpolation and also for the numerical calculation of time derivatives have been tried. The final results do not significantly depend on the chosen methods because these results depend much more on the simulation resolution (see comments on Fig. (6) given below). Two types of spatial interpolations have been considered: (i) an standard 3D linear interpolation using the potential in the eight nodes of the P cell, and (ii) a 3D interpolation based on the use of splines along each direction;

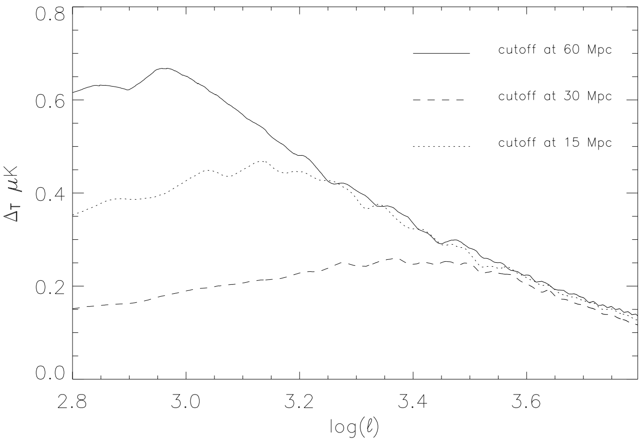

Figure 5. RS power spectrum, Δ_T, in μK, as a function of $\log(\ell)$. Solid, dotted and dashed lines are the spectra produced by spatial scales smaller than 60 *Mpc*, 30 *Mpc*, and 15 *Mpc*, respectively. IR simulations have been used.

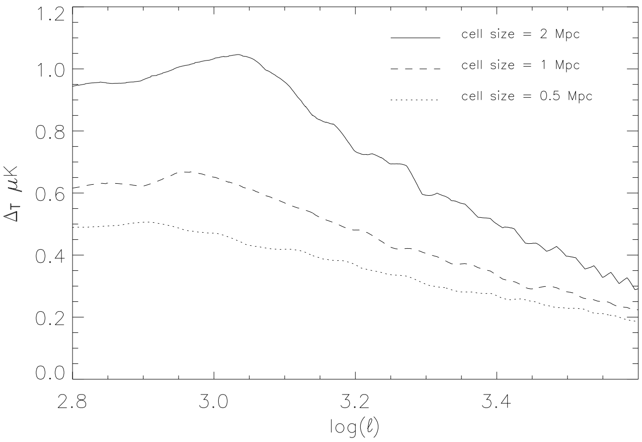

Figure 6. RS power spectrum, Δ_T, in μK, as a function of $\log(\ell)$. Solid, dashed and dotted lines are the spectra obtained from the LR, IR, and HR simulations defined in the text, respectively. Scales are smaller than 60 *Mpc* in all cases.

in this case, four vertices located in the P-cell and in their neighbouring ones are considered for interpolations in the directions of the box edges; results from both interpolations are very similar; relative differences between the C_ℓ coefficients extracted from the maps obtained with the two interpolations are smaller than 0.02 for any ℓ. Also time derivatives based on different numbers of points, η_i, have been performed, but the results are almost identical in all cases because ϕ is a very smooth function of η in any node of the simulation grid (see Aliaga, Quilis & Sáez (2002)). In short, a 3D linear interpolation in space and a standard derivative based on two times η_i and η_{i+1} suffice to get good maps of the RS effect. Various methods have been also used to perform the integral in Eq. (1): trapezoidal, Simpson, and so on. Results are almost identical in all cases. All these comments show that our ray-tracing procedure is a robust numerical method, which leads to RS maps having almost the same properties for a wide set of numerical techniques (interpolations, derivatives and integrations).

4 ON THE ANGULAR POWER SPECTRUM OF THE RS EFFECT

Since we are concerned with small squared regularly pixelised maps, the power spectrum estimator described in Arnau, Aliaga & Sáez (2002) applies. Although this estimator is used as the basic one along the paper, some results are compared with those of the code ANAFAST included in the HEALPIx package.

The basic estimator is first used to analyze $1.83^\circ \times 1.83^\circ$ RS maps obtained from IR simulations with $L = 256$ *Mpc*. Figure 5 shows the resulting angular power spectra (Δ_T) for three appropriate choices of the cutoff: 60, 30, and 15 *Mpc*. Differences between the Δ_T values corresponding to the solid (dotted) and dotted (dashed) lines are produced by scales between 60 and 30 *Mpc* (30 and 15 *Mpc*). The relation $\Delta_T > 0.037$ μK is satisfied and, according to previous comments (see section 2), the ISW effect cannot produce these spectra; therefore, scales between 60 *Mpc* and 15 *Mpc* seem to produce a certain Rees-Sciama effect, which is only possible if they become non-linear enough in our simulation boxes. The question is: are the scales between 15 and 60 *Mpc* well described in our simulations? In order to answer, it should be taken into account that the evolution of the scales under consideration depend on N-body simulation characteristics as resolution and box size; indeed, the greater the N-body resolution, the better (more realistic) the description of all the spatial scales and, in particular, the description of the scales between 15 and 60 *Mpc*. We can say then that part of the non-linear behaviour of these scales is due to low resolution (see next paragraph for more discussion).

For a cutoff at 60 *Mpc* and a fixed box size $L = 256$ *Mpc*, the angular power spectrum of the RS maps has been calculated for HR, IR, and LR simulations; namely, for different space and mass resolutions. The resulting spectra are displayed in Fig. 6, where we see that the greater the resolution the smaller the amplitude of the RS effect. Taking into account Fig. 5 this behaviour of the amplitude is not surprising because, as resolution increases, the evolution of the scales between 60 and 15 *Mpc* is better described and masses concentrate more and more on smaller and smaller scales. Taking into account that the separation between the solid and dashed lines is greater than that of the dashed and dotted lines, it seems that, although the spectra of Fig. 6 depend on resolution, they tend to a certain spectrum located below the dotted line and close to it; hence, this line gives an upper limit to the true spectrum. The difference between the true spectrum and the upper limit (dotted line) is expected to be small and, consequently, the dotted line can be considered as our best estimation of the RS angular power spectrum. In spite of this fact, there are systematic errors in this spectrum associated to the smallness of our simulated maps. These errors are analyzed below

The spectra of Fig. 6 have been obtained for an initial redshift $z_{in} = 5.2$, but other initial redshifts have been tried. Fig. 7 shows the spectra obtained from initial redshifts of 5.2, 10.2 and 15.2. In the three cases, IR simulations have been used and the size of the simulated maps is $1.83^\circ \times 1.83^\circ$. In order to maintain the map area for the three initial redshifts, the size of the simulation box (and accordingly the

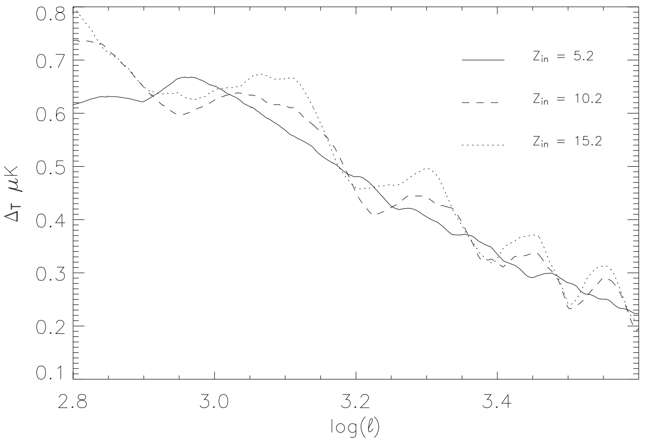

Figure 7. RS power spectrum, Δ_T, in μK, as a function of log(ℓ). Solid, dashed, and dotted lines correspond to the spectra obtained from the initial redshifts 5.2, 10.2, and 15.2, respectively. IR simulations and scales smaller than 60 Mpc have been considered in the three cases.

resolution) has been varied. The assumed box size (N-body resolution) slightly increases (decreases) as the initial redshift grows. Figure 7 shows oscillations in Δ_T whose amplitude increases as z_{in} does. In spite of these unexplained oscillations, the resulting spectra are rather similar in the three cases and, as it follows from this figure, the choice of the initial redshift $z_{in} = 5.2$ is the simplest one leading to a good estimate of Δ_T without spurious oscillations.

The spectra obtained from our small non-Gaussian RS maps have systematic errors which are now approximately estimated. In order to perform this estimation, we begin with the analysis of Gaussian maps of the same size and, then, results are considered as an approximated estimate of the errors associated to the non-Gaussian RS simulations. This procedure seems to be reasonable taking into account that deviations from Gaussianity of the RS maps do not seem to be dramatic (see our discussion in section 5). As it is well known, the relative errors of the C_ℓ quantities extracted from a Gaussian map is $\Delta C_\ell / C_\ell = [2/(2\ell+1)]^{1/2} f_{sky}^{-1/2}$, where f_{sky} is the ratio between the map area and that of the full sky (Scott, Sredniki & White 1994; Knox 1995). According to this formula, the relative errors corresponding to $3.66^\circ \times 3.66^\circ$ Gaussian maps range between ~ 2.5 and ~ 0.5 as ℓ takes on the values of the interval $(500, 10000)$. For $1.83^\circ \times 1.83^\circ$ ($7.2^\circ \times 7.2^\circ$) maps these errors increase (decrease) by a factor 2. These relative errors are so large that one could think that Gaussian maps of dominant anisotropy (and also our simulated maps) are not useful at all; however, when C_ℓ quantities are extracted from one of the mentioned Gaussian maps, the errors lead to a oscillatory angular spectrum which changes from ℓ to $\ell + 1$; in other words, the resulting spectrum has high frequency oscillations which can be eliminated by means of suitable averages. These averages are performed during (after) the C_ℓ estimations when the method proposed in Arnau, Aliaga & Sáez (2002) (ANAFAST) is used. The final averaged spectra are meaningful in a certain interval of ℓ values. In order to define this interval, $1.83^\circ \times 1.83^\circ$ maps of the CMB dominant anisotropy have been simulated by using: the angular power spectrum given by CMBFAST (in the model assumed here) and a map making method based on the fast Fourier transform Sáez, Holtmann & Smoot (1996). The resulting maps are analyzed with two different power spectrum estimators. In the top panel of Fig. 8, the solid line is the CMBFAST spectrum used as input in the simulated maps, the dashed line is the spectrum extracted from the maps by using the power spectrum estimator described in Arnau, Aliaga & Sáez (2002) and, finally, the dotted line has been obtained using ANAFAST (see above) to analyze an equatorial healpix map obtained from our uniformly pixelised one. Both estimators give very similar spectra which

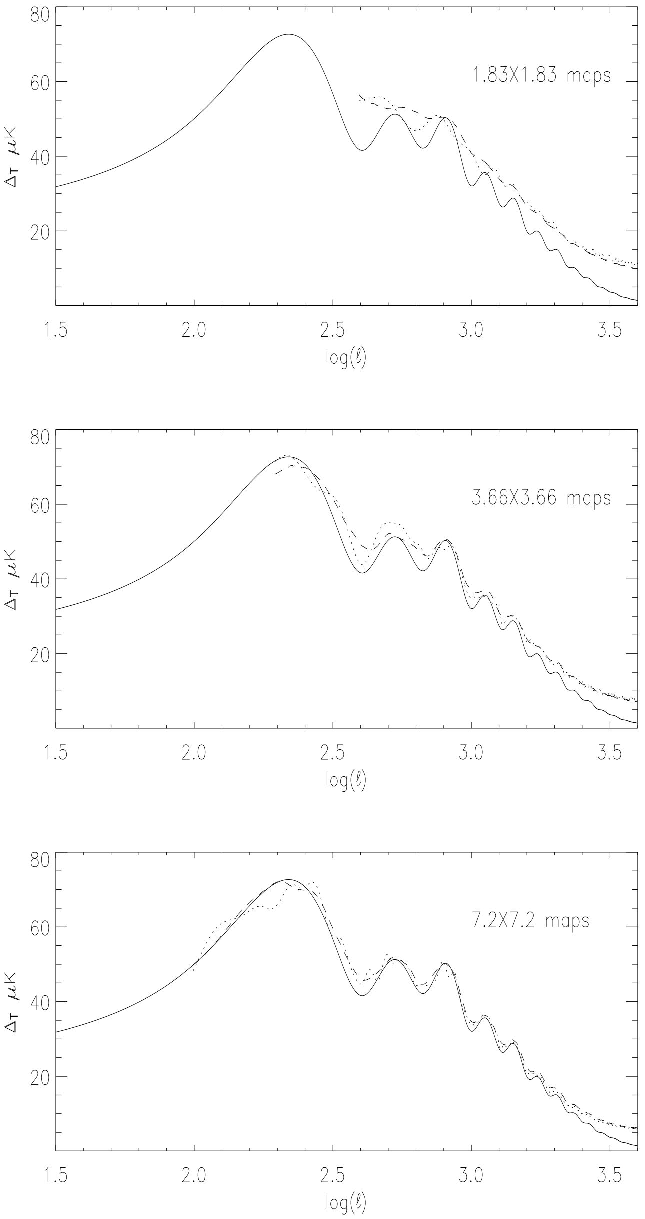

Figure 8. CMB power spectrum, Δ_T, in μK, as a function of log(ℓ) in all panels. All the solid lines exhibit the CMB spectrum given by CMBFAST which is used as an input to simulate CMB maps. Top, middle, and bottom panels correspond to $1.83^\circ \times 1.83^\circ$, $3.66^\circ \times 3.66^\circ$, and $7.2^\circ \times 7.2^\circ$ maps, respectively. In the three panels, dotted and dashed lines are the spectra extracted from the simulated maps by using two distinct estimators (see text).

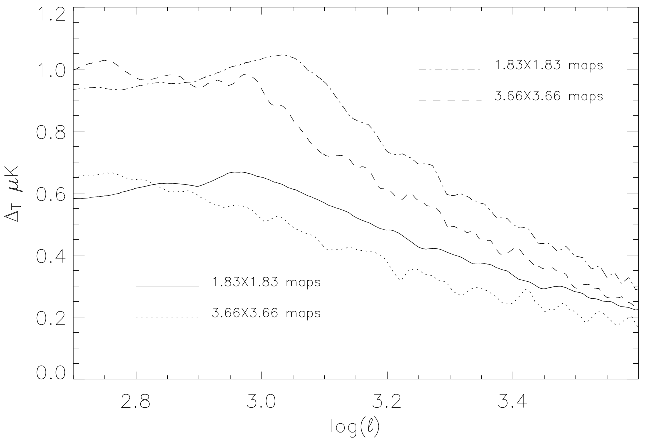

Figure 9. RS power spectrum, Δ_T, in μK, as a function of $\log(\ell)$. Dotted-dashed and dashed (solid and dotted) lines have been obtained with LR (IR) simulations for $L = 256$ Mpc and $L = 512$ Mpc, respectively. The angular sizes of the maps are given inside the panel. Scales are smaller than 60 Mpc in all cases.

can be considered as a rather good estimate of the true spectrum for $500 \leqslant \ell \leqslant 2000$. Maps are too small to get the spectrum for $\ell < 500$ and, furthermore, for $\ell > 2000$, the signal is too weak and, then, numerical and statistical noise become comparable to it. The middle and bottom panels of Fig. 8 have the same structure as the top panel; however, in the middle (bottom) panel the angular size of the maps is 3.66° × 3.66° (7.2° × 7.2°). Comparing the panels of Fig. 8, one concludes that the more extended the maps, the better the resulting spectra and the wider the ℓ interval where the spectra are good enough. In the case of the RS effect studied with HR simulations, the size of our simulation boxes ($L = 256$ Mpc) and, consequently, the angular size of the resulting maps (1.83° × 1.83°) cannot be freely increased because any significant increment would lead to a problematic decrease of the N-body simulation resolution, nevertheless, if the above results corresponding to Gaussian maps are applied –as an approximation– in the presence of deviations from Gaussianity, our 1.83° × 1.83° maps should suffice to get a rough, but useful, estimate of the RS spectrum in a wide ℓ interval. This conclusion is confirmed by a direct study of RS maps presented in the next paragraph.

In order to have direct information about the quality of the spectra associated to 1.83° × 1.83° RS maps, two tests have been performed. In the first one, maps of this angular size have been obtained from LR simulations with $L = 256$ Mpc and, then, the angular power spectrum extracted from these maps (which is presented in the dashed-dotted line of Fig. 9) is compared with that obtained from LR simulations with $L = 512$ Mpc which lead to 3.66° × 3.66° RS maps (dashed line of the same Figure). Since both simulations have the same resolution, differences in the resulting spectra are due to the difference between the angular size of the maps. The comparison of the dashed-dotted and dashed lines of Fig. 9 shows that, in the 1.83° × 1.83° maps, the spectrum is slightly underestimated for $500 < \ell < 800$ and overestimated for $\ell > 800$. The second test is identical to the first one except for the resolution of the involved simulations. The 1.83° × 1.83° maps are obtained with IR simulations and $L = 256$ Mpc, and the maps whose angular size is 3.66° × 3.66° are created with IR simulations in boxes with $L = 512$ Mpc; the corresponding spectra are displayed by the solid and dotted lines of Fig. 9, respectively. The comparison of these spectra indicates that, for the smallest maps, the resulting spectrum is underestimated (overestimated) for $500 < \ell < 700$ ($\ell > 700$). Furthermore the maxima of the dashed-dotted and solid lines appear as a result of the overestimations and they disappear in the case of our most extended maps (see the dotted and dashed lines). Unfortunately, HR simulations cannot be used to perform a third test similar to the previous ones (too great computational cost of HR simulations with $L = 512$ Mpc), nevertheless, previous discussion strongly suggests that, also in the case of 1.83° × 1.83° RS maps generated with HR simulations, the spectrum (dotted line of Fig. 6) should be underestimated and overestimated as in the first and second tests (see the weak maximum observed in that dotted line); therefore, for $\ell > 800$, the Δ_T quantities corresponding to 3.66° × 3.66° HR maps should be smaller than those extracted from 1.83° × 1.83° HR maps (dotted line of Fig. 6). In other words, the smallness of the maps leads to an overestimation of the angular power spectrum for large ℓ values.

Previous discussion about the Δ_T uncertainties associated to both N-body resolution (Fig. 6) and map size (Fig. 9) can be summarized as follows: (1) for ℓ values between 700 and 800, the spectrum Δ_T slightly depends on the map size (see Fig. 9); however, its dependence on N-body resolution (see Fig. 6) is important; hence, the Δ_T value corresponding to $\ell \simeq 700$ essentially depends on resolution. From the visual analysis of Fig. 6 one easily concludes that this value should be a number between 0.4 μK and 0.5 μK, (2) for $\ell > 800$, the overestimations of Δ_T associated to N-body resolution and map size are comparable and they add to generate a total excess of power which might be close to 0.2 μK. This number follows from a qualitative study of Figs. 6 and 9, (3) on account of points (1) and (2), the dotted line of Fig. 6 appears to be an upper limit to the RS spectrum, but it can be considered, in practice, as an useful rough estimation of the true spectrum. The most important point is that the resulting spectrum has been obtained from fully nonlinear dark matter evolution (without approximating techniques o models), and (4) more resolution and more extended maps are necessary to get a more accurate RS spectrum.

5 STATISTICAL ANALYSIS

Various reduced correlation functions are estimated and then deviations from Gaussianity are analyzed. The correlations associated to n directions (or n points on the last scattering surface) are estimated for $n \leqslant 6$. Given a map of the variable ζ, and m directions, the reduced angular correlations are:

$$C_m = \langle \zeta(\vec{n}_1) \zeta(\vec{n}_2) \cdots \zeta(\vec{n}_m) \rangle \ , \tag{12}$$

where the average is over many statistical realizations.

Correlations depend on the relative positions of the chosen directions; hence, for CMB and RS maps, they depend on the figures that these directions draw on the last scattering surface. In this paper we have used the sets of directions

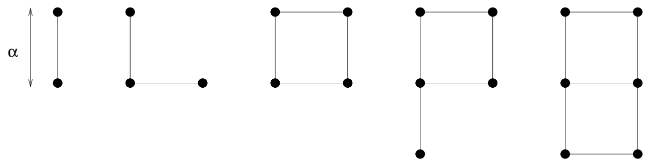

Figure 10. m-direction configurations for statistical analysis

displayed in Fig. 10, where the basic correlation angle, α, is that subtended by the two directions of the case $n = 2$. In Gaussian statistics it is well known that (Peebles 1980): (i) all the C_m correlations vanish for odd m and, (ii) for even m, all the correlations can be written in terms of C_2. Hereafter, these even Gaussian correlations are denoted C_{gm} (the suffix g stands for Gaussian). For the configurations of Fig. 10, one easily obtains the relation:

$$C_{g4}(\alpha) = 2C_2^2(\alpha) + C_2^2(\sqrt{2}\alpha) \ , \tag{13}$$

leading to $C_{g4}(0) = 3C_2^2(0)$ for $\alpha = 0$, and the equation:

$$\begin{aligned} C_{g6}(\alpha) &= 3C_2^3(\alpha) + 2C_2(\alpha)C_2^2(\sqrt{2}\alpha) \\ &+ 4C_2(\alpha)C_2(2\alpha)C_2(\sqrt{2}\alpha) \\ &+ 2C_2(\sqrt{5}\alpha)C_2^2(\sqrt{2}\alpha) + C_2(\alpha)C_2^2(\sqrt{5}\alpha) \\ &+ 2C_2(\sqrt{5}\alpha)C_2^2(\alpha) + 2C_2(\alpha)C_2^2(2\alpha) \ , \end{aligned} \tag{14}$$

which takes on the form $C_{g6}(0) = 15C_2^3(0)$ for $\alpha = 0$. Our RS simulated maps are not Gaussian and we are interested in deviations from Gaussianity. Even correlations can be used to estimate these deviations as follows: (a) extract the C_2, C_4, and C_6 correlations from the simulated maps, (b) use the extracted C_2 correlation to calculate C_{g4}, and C_{g6} functions assuming Gaussianity, namely, using Eqs. (13)–(14) and, (c) compare C_4 and C_6 correlations with functions C_{g4} and C_{g6}, respectively. Differences between C_4 and C_{g4} as well as between C_6 and C_{g6} measure deviations from Gaussianity. Furthermore, odd correlations vanish in the Gaussian case and, consequently, if at least one of the correlations C_3 and C_5 (for the configurations of Fig. 10) appears to be different from zero, we can conclude that the analyzed RS maps are not Gaussian.

In order to get the C_m correlation from a set of maps, the m-configuration of Fig. 10 is randomly placed on the maps and, then, the temperature contrasts in the nodes of the configuration are calculated by appropriate interpolations in our maps (making use of their pixelisation); finally, the average of Eq. (12) is calculated considering all the maps and all the locations of the m-configuration. As it occurs in the case of the C_ℓ quantities, the fact that our simulated maps are small implies that the C_m correlations extracted from them are not the true ones. In spite of this fact, it is now proved that the methods proposed above to detect deviations from Gaussianity –based on the use of even correlations– work. In order to do that, these methods are first applied to CMB maps –Gaussian by construction– having either the same sizes as our simulated RS maps or larger ones; in this way, small Gaussian maps are characterized and, then, deviations of the RS maps with respect to this characterization point out a certain level of non-Gaussianity.

We begin with $1.83^\circ \times 1.83^\circ$ Gaussian CMB maps. Some correlations extracted from these maps are displayed in the panels of Fig. 11. The dashed (dashed-dotted) line of the top panel exhibits the C_4 (C_{g4}) correlations (see above), whereas the same lines of the bottom panel display C_6 and C_{g6} correlations. Since the $1.83^\circ \times 1.83^\circ$ maps are too small, correlations extracted from them are not the true correlations (which could be obtained from a large set of big maps) and, consequently, in spite of Gaussianity, functions C_4 and C_{g4} slightly separate (compare dashed and dashed-dotted lines in the top panel of Fig. 11). The same occurs for the correlations C_6 and C_{g6} (compare dashed and dashed-dotted lines in the bottom panel of Fig. 11). In the case of $3.66^\circ \times 3.66^\circ$ maps, the correlations are presented in Fig. 12 using the same notation as in Fig. 11. From Fig. 12 one easily concludes that dashed and dashed dotted lines are much closer than in the corresponding panels of Fig. 11. It has been verified that for $7.2^\circ \times 7.2^\circ$ maps, the corresponding lines are closer than in Fig. 12. This behaviour characterize Gaussian maps, in which the C_4 and C_6 correlations approach the C_{g4} and C_{g6} functions, respectively, as the map size increases and the extracted correlations approach more and more the true ones. It is worthwhile to notice that, although the cor-

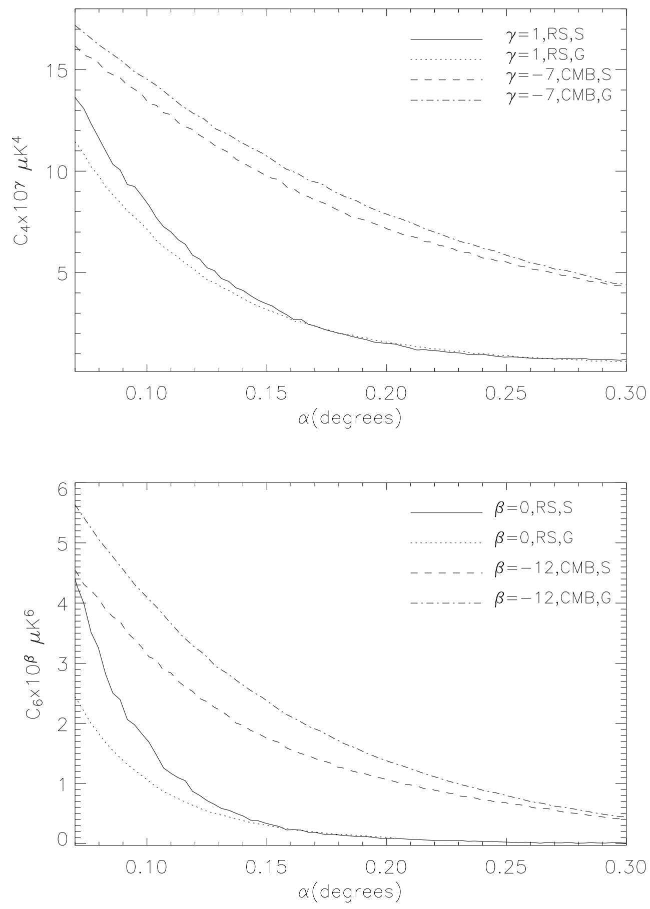

Figure 11. Even correlation functions obtained from $1.83^\circ \times 1.83^\circ$ maps in terms of the correlation angle α. C_4 (C_6) correlations are multiplied by an appropriate power of ten and given in μK^4 (μK^6). Top (bottom) panel corresponds to C_4 (C_6) functions. Dashed-dotted (dashed) line exhibits either C_{g4} or C_{g6} (C_4 or C_6) correlations extracted from CMB maps. Solid (dotted) line shows either C_{g4} or C_{g6} (C_4 or C_6) correlations found from RS maps. Each type of line is defined inside the panel giving: (i) the power of ten exponent, (ii) the type of map (CMB or RS), and (iii) the type of correlation (S, for C_4 and C_6, and G, for C_{g4} and C_{g6})

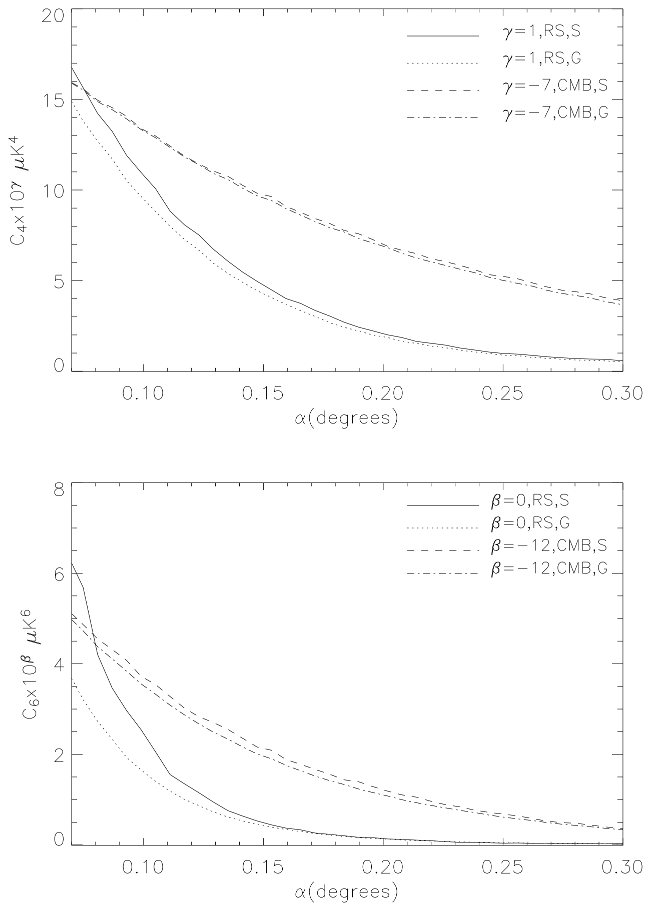

Figure 12. Same as in Fig. 11 for 3.66° × 3.66° maps

relations C_2, C_4 and C_6 obtained from small maps are not the true correlations, they allow us to verify the Gaussian behaviour described above, which can be applied to detect deviations from Gaussianity.

Even correlations extracted from 1.83° × 1.83° and 3.66° × 3.66° RS maps are now analyzed. In order to do that, the study described in the last paragraph (for CMB maps) is repeated for RS maps. Results are also presented in Figs. 11 and 12; in which solid and dotted lines are used to represent the same correlations given by the dashed-dotted and dashed lines of the same Figures (see above). From the comparison of the solid and dotted lines one easily concludes that: (i) for 1.83° × 1.83° maps (Fig. 11), these lines separate for $0.07^\circ < \theta < 0.15^\circ$. Since this separation is comparable to that corresponding to Gaussian CMB small maps (dashed-dotted and dashed lines), it does not point out any deviation from Gaussianity, and (ii) for 3.66° × 3.66° maps (Fig. 12), the separation between solid and dotted lines is much greater than that of the CMB Gaussian maps with the same size (dashed dotted and dashed lines of Fig. 12). It occurs for all the angular scales we have represented, which include the scales corresponding to $500 < \ell < 2000$, for which ou best estimation of the RS spectrum (dotted line of Fig. 6) has been obtained. This result (great separation) proves that the RS maps are not Gaussian because, in the case of Gaussianity, the separation of the solid and dotted curves corresponding to 3.66° × 3.66° maps must be smaller than the separation corresponding to 1.83° × 1.83° maps (Gaussian behaviour defined above).

Odd correlations have been also considered. Maps of 1.83° × 1.83° and 3.66° × 3.66° squared degrees have been used to study these correlations. In the case of CMB Gaussian simulations, the general method (see above) for estimating functions C_3 and C_5 has been applied using n small CMB maps. Different n values have been considered. Results do not converge as n increases because the true odd correlations vanish and, consequently, the functions C_3 and C_5 extracted from n simulated Gaussian CMB maps are pure errors for any n. This complete absence of convergence characterizes small Gaussian maps for any size. In the case of RS small maps with any of the above sizes, it has been verified that the C_3 and C_5 correlations extracted from a number m of these maps do not converge as m-increases (as it occurs for Gaussian maps); this means that we have not been able to detect the small odd correlations associated to the RS effect (see next section for more discussion).

6 RESULTS AND DISCUSSION

In this paper, an improved version of the numerical methods used in Aliaga, Quilis & Sáez (2002) is applied to study the RS effect. Our main improvements: preferred direction and appropriate cutoff were described in Cerdá-Durán, Quilis & Sáez (2004) and successfully applied in Antón et al. (2005). These new elements make negligible the magnification of the RS and lens effects due to the spatial periodicity of the simulated universe, which is covered by identical simulation boxes. The present size of these boxes must range between $\sim 256\ Mpc$ and $\sim 512\ Mpc$. Only in this way, good N-body simulations with large enough resolutions can be obtained using our PM code; as a result of this size restriction, we are constrained to work with small maps of the RS effect having sizes between 1.83° × 1.83° and 3.66° × 3.66° (see section 3). Since the correlations obtained from these small maps are expected to have important uncertainties, an exhaustive study about the accuracy and significance of these correlations is developed. Furthermore, methods specially designed for detecting deviations with respect to Gaussianity (using the correlations of small maps) are described and applied.

The analysis of small CMB Gaussian maps of dominant anisotropy (CMBFAST angular power spectrum, see section 4) has been basic in order to study both power spectrum estimations and non-Gaussianity detection. The following studies have been developed: (1) the C_ℓ quantities extracted from Gaussian CMB maps (for different sizes) have been compared with those used in their simulation; in this way, the interval (ℓ_1,ℓ_2) where the recovered angular power spectrum is good enough (from a qualitative point of view) has been estimated (see Fig. 8 of section 4), the existence of this interval has been interpreted taking into account the concept of sample variance and, (2) the method described in section 5 to look for deviations with respect to Gaussianity –from even correlations– has been applied to analyze CMB maps with distinct sizes and, thus, Gaussian maps have been characterized, which has been basic for further researches about deviations from Gaussianity. The interval (ℓ_1,ℓ_2) depends on the map size (see section 4) and the C_ℓ quantities have been calculated for various of these sizes. The larger the size of the RS map, the wider this interval. More extended maps are necessary to get the angular power spectrum for $\ell < \ell_1$, and more extended maps and greater resolutions are needed to find this spectrum in the case $\ell > \ell_2$; namely, for very small angular scales. There is the opinion that the RS effect could produce some feature in the angular power spectrum at small enough angular scales, by this reason, our main project in this field is the use of P3M and AP3M N-body codes to get resolutions as high as possible in large enough boxes. In spite of this plan, we are skeptical about the existence of the mentioned feature because the RS effect is produced by the time derivative of the peculiar potential, which seems to be rather well estimated with the effective resolution of 1 Mpc corresponding to the dotted line of Fig. 6, in which, there is no any trace of incipient features at large ℓ values; nevertheless, it must be recognized that, for these large values, the uncertainties in our spectrum are maximum (superimposition of the overestimations due to resolution and map smallness) and, consequently, a moderated excess of power due to fully non-linear evolution could be hidden by our current uncertainties. Our method (based on N-body simulations) is fully nonlinear and, moreover, it takes into account both the effect due to the gravitational collapse of cosmological structures and that produced by the motion of these structures in the box. These are the most promising aspects of the proposed techniques whose future applications –based on better N-body simulations and computers– can improve on both the estimation of the RS spectrum (pointing out posible new features) and the detection of deviations from Gaussianity. In other words, although improvements on the applications of the ray tracing procedure used here are possible, current applications lead to too small RS maps and moderate N-body resolutions and, consequently, only an upper limit to the RS spectrum (rough estimate of it) has been obtained in this paper. Fortunately, we are going to see that this estimate suffices to discuss detection of the RS effect with WMAP and PLANCK satellites (see below) and, furthermore, our detection of deviations from Gaussianity in RS maps seems to be doubtless.

A few comments about previous results are now necessary for comparisons. The angular power spectrum of the Rees-Sciama effect was studied by Tuluie, Laguna & Anninos (1996) and Seljak (1996). In both papers, the effect was estimated for open and flat cold dark matter universes without cosmological constant. In the first of these papers, the authors used N-body simulations and a certain ray-tracing procedure to get the C_ℓ coefficients for $\ell < 700$. Among their results we emphasize the following ones: (α) in the case of a flat universe (with h=0.75 and $\sigma_8 = 1$), and for ℓ close to 700, quantity Δ_T takes on values around 0.27 μK, and (β) for $\ell \sim 100$ this quantity reaches a maximum value close to 0.85. In the second paper, Seljak (1996) did not use any ray tracing procedure. He used N-body simulations (second order perturbation theory) to evolve the density contrast of strongly (mildly) non-linear structures and, then, from the resulting contrast, the author estimated the power spectrum of the quantity $\partial\phi(\vec{x},t)/\partial t$. Finally, from this spectrum, the C_ℓ quantities were calculated. Four cases corresponding to different values of the parameters σ_8 and $\Omega_m h$ were studied using N-body simulations. Some results corresponding to these four cases are now summarized: (i) the temperature contrast ($\Delta T/T$) takes on values between 10^{-6} and 10^{-7}, (ii) quantity Δ_T is maximum between $\ell = 100$ and $\ell = 300$, (iii) the maximum values of Δ_T range from 0.38 μK to 2.25 μK and, (iv) the values corresponding to $\ell \sim 700$ ranges from 0.27 μK to 1.2 μK (the first of these values corresponds to a flat universe with h=0.5 and $\sigma_8 = 0.6$). More recently, the RS effect has been estimated, in the concordance model, for various slightly different values of the involved parameters (see, e.g. Cooray (2002) and Hu & Dodelson (2002)); these estimations are not based on N-body simulations and they lead to small values of Δ_T for $\ell \simeq 700$; these values are ~ 0.17 μK in Cooray (2002) and ~ 0.2 μK in Hu & Dodelson (2002). As it has been discussed in section 4, the value of C_{700} extracted from our small RS simulations seems to be between 0.4 μK and 0.5 μK; this approximated value seems to be a little greater than those found (with other models and methods) by Tuluie, Laguna & Anninos (1996), Seljak (1996), Cooray (2002), and Hu & Dodelson (2002). The Δ_T spectrum given in the three last of these references and that obtained by us slowly decrease for $\ell > 700$; nevertheless, our spectrum decreases slower than that shown in Cooray (2002) and Hu & Dodelson (2002). Our Δ_T overestimations, at large ℓ values, associated to map smallness (see section 4) seem to explain this difference.

The C_3 correlation induced by the RS effect was studied by Mollerach et al. (1995) and Munshi, Souradeep & Starobinski (1995). The main conclusion of these authors was that this odd correlation is smaller than its cosmic variance, which suggests that it is too small to be detected from a unique complete realization of the RS sky. Of course, we have not any map of the full sky, but very small maps of the RS effect and, consequently, it should not be possible the estimation of C_3 from these small parts of the full sky. In spite of these considerations and taking into account that the mentioned estimates of C_3 are based on perturbation theory, which does not properly describe strong non-linear evolution inside cluster and substructures, we have tried the estimation of the C_3 and C_5 correlations from our 1.83° × 1.83° and 3.66° × 3.66° RS maps; nevertheless, this estimate has not been possible, which confirms the low level of these odd correlations in the maps of the RS effect.

Even correlations have been calculated for both CMB and RS small maps and, after comparisons, a certain deviation with respect to Gaussianity has been pointed out in the RS case (see section 5); however, no deviations have appeared in the analysis of the superimposition of RS and CMB maps. It is due to the fact that the RS non-Gaussian part is much smaller than the CMB Gaussian one. The superimposition is almost Gaussian and, consequently, cosmic variance errors, $\Delta C_\ell = [2/(2\ell+1)]^{1/2} C_\ell$, are a good approximation to the C_ℓ uncertainty in full sky measurements. These errors can be easily calculated taking into account that the angular power spectrum of the superimposition is almost identical to that of pure CMB. In the ℓ interval [500,2000], where we have found our best estimate of the RS spectrum (see section 4), one easily finds the errors of Δ_T, in μK, associated to cosmic variance. They are displayed in the solid line of Fig. 13. In the same Figure, the dotted line is our best estimate of the RS spectrum (also represented

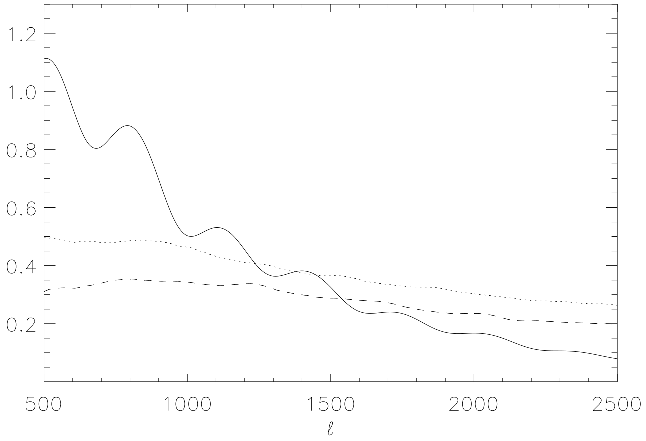

Figure 13. numbers in the vertical axis are temperatures in μK. The solid line displays the errors of Δ_T due to cosmic variance and the dotted (dashed) line is the spectrum Δ_T obtained from HR simulations for $\sigma_8 = 0.93$ ($\sigma_8 = 0.76$)

in the dotted line of Fig. 6), and the dashed line is a new spectrum which has been obtained using the same method as in the case of the dotted line, but assuming $\sigma_8 = 0.76$ in our HR simulations. This new normalization is suggested by the analysis of the three year WMAP data published (Spergel et al. 2006) after the submission of the first version of this paper. In Fig. 13 we see that, for the two σ_8 values we have considered, our upper limits to the RS spectrum are well below the cosmic errors for $\ell < 1200$; hence, taking into account that WMAP cannot accurately measure C_ℓ coefficients for $\ell > 1200$ (see Hinsaw et al. (2006)), one easily concludes that the RS effect cannot be observed with this satellite. Finally, the upper limits to the RS spectrum displayed in the dotted and dashed lines are well above Δ_T errors for $1500 < \ell < 2000$; however, taking into account that the true RS spectra are expected to be around 0.2 μK smaller than our upper limits for large ℓ values (see section 4), it follows that the true Δ_T values are not expected to be greater than the cosmic errors given by the solid line of Fig. 13. This means that, although all the multipoles up to $\ell \simeq 2500$ could be measured with PLANCK, the RS effect would be too small to be detected with this satellite. All these considerations strongly suggest that the RS effect will not be directly detected in the near future. Indirect detection based on correlations of the CMB with the cluster distribution producing the effect deserves attention.

Simulations in great boxes would lead to more extended RS maps (improving on power spectrum estimation and non-Gaussianity detection). In the case of large simulation boxes with $L \simeq 1000\ Mpc$, which can be currently considered with appropriate N-body codes and computers, the magnification of the RS effect associated to periodicity is not negligible because eight of these boxes are yet necessary to cover the photon trajectory from $z = 5.2$ to present time. Of course, our method based on a preferred direction also applies for these big boxes. After minimum changes, our codes will be ready to built up better RS maps from appropriate N-body simulations, and also to statistically analyze these maps.

ACKNOWLEDGMENTS

This work has been supported by the Spanish MEC (project AYA2003-08739-C02-02 partially funded with FEDER) and also by the Generalitat Valenciana (grupos03/170). Calculations were carried out at the Centro de Informática de la Universidad de Valencia (CERCA and CESAR).

REFERENCES

Afshordi N., Lho Y-S., Strauss M.A., 2004, Phys. Rev. 69D, 3524
Aliaga A.M., Quilis V., Sáez D., 2002, MNRAS, 330, 625
Antón L., Cerdá-Durán P., Quilis V., Sáez D., 2005, ApJ, 628, 1
Arnau J.V., Aliaga A.M., Sáez D., 2002, A&A, 382, 1138
Bennet C.L. et al., 2003, ApJS, 148, 1
Boughn S.P., Crittenden R.G., 2004, Nat, 427, 45
Cerdá-Durán P., Quilis V., Sáez D., 2004, Phys. Rev., 69D, 043002
Cooray, A., 2002, Phys. Rev. 65D, 103510
Cooray, A., 2002, Phys. Rev. 65D, 083518
Crittenden, R.G., Turok, N., 1996, Phys. Rev. Lett., 76, 575
Eke, V., Cole S., Frenk C.S., 1996, MNRAS, 282, 263
Fosalba P., Gaztañga, E., Castander F., 2003, ApJ, 597, L89
Fosalba P., Gaztañga, E., 2004, MNRAS, 350, 37
Fullana M.J., Sáez D., 2000, New Astronomy, 5, 10
Górski, K.M., Hivon, E., Wandelt, B.D., 1999, Proceedings of the MPA/ESO Conference on Evolution of Large Scale Structure, Eds. Banday, A.J., Sheth, R.K., & Da Costa, L., [astro-ph/9812350]
Hinsaw, G. et al., 2006, astro-ph/0603451
Hockney R.W., Eastwood J.W., 1988, Computer Simulations Using Particles (Bristol: IOP Publisings)
Hu W., Dodelson S., 2002, Annu. Rev. Astron. Astrophys., 40, 171
Jain B., Seljak U., White S., 2000, ApJ, 530, 547
Knox L., 1995, Phys. Rev., 52D, 4307
Martínez-González E., Sanz J.L., Silk J., 1990, ApJ, 355, L5
Mollerach S., Gangui A., Lucchin F., Matarrese S., 1995, ApJ, 453, 1
Munshi D., Souradeep T., Starobinski A.A., 1995, ApJ, 454, 552
Nolta et al., 2004, ApJ, 608, 10
Padmanabhan, N., Hirata, C.M., Seljak, U., Schlegel, D.J., Brinkmann, J., Schneider, D.P., 2005, Phys. Rev., 72D, 043525
Peebles P.J.E., 1980, The Large Scale Structure of the Universe, Princeton University press, Princeton
Quilis V., Ibáñez J.M., Sáez D., 1998, ApJ, 502, 518
Sáez D., Holtmann E., Smoot G.F., 1996, ApJ, 473, 1
Scott D., Sredniki M., White M., 1994, ApJ, 421, L5
Seljak U., 1996, ApJ, 463, 1
Seljak U., Zaldarriaga M., 1996, ApJ, 469, 437
Spergel, D.N. et al., 2006, astro-ph/0603449
Tuluie R., Laguna P., Anninos P., 1996, ApJ, 463, 15
Vielva, P., Martínez-González, E., Tucci, M., 2006, MNRAS, 365, 891

White M., Hu W., 2001, ApJ, 537, 1

This paper has been typeset from a TEX/ LATEX file prepared by the author.